Advanced Ceramics Progress: Vol. 11, No. 2, (Spring 2025) 24-35

Materials and Energy Research Center
MERC

Contents lists available at ACERP

Advanced Ceramics Progress

Journal Homepage: www.acerp.ir

Original Research Article

Multiferroic Performance of BCZT/CFO Composites Tailored by Antimony and Yttrium Doping

Ali Sharifi [a], Raziye Hayati [b,*], Nader Setoudeh [b], Ghasem Rezaei [c]

[a] *MS, Department of Materials Engineering, Faculty of Engineering, Yasouj University, Yasouj, Iran*
[b] *Associate Professor, Department of Materials Engineering, Faculty of Engineering, Yasouj University, Yasouj, Iran*
[c] *Professor, Department of Physics, Yasouj University, Yasouj, 75918-74934, Iran*

* Corresponding Author Email: r.hayati@yu.ac.ir (R. Hayati) URL: https://www.acerp.ir/article_238621.html

ARTICLE INFO

Article History:

Received 05 October 2025
Revised 01 November 2025
Accepted 02 January 2026

Keywords:

Chemical Synthesis
Ferroelectric
Magnetic
Composite
$CoFe_2O_4$
$Ba_{0.85}Ca_{0.15}Zr_{0.1}Ti_{0.9}O_3$
Doping

ABSTRACT

In this research, magnetic CoFe2O4 (CFO) and ferroelectric Ba0.85Ca0.15Zr0.1Ti0.9O3 (BCZT) compounds were synthesized via combustion and sol-gel methods, respectively. The influence of antimony and yttrium oxides on the electrical and magnetic properties of these two compounds was investigated. Following the selection of an appropriate dopant from these two additives, the composite materials were subsequently fabricated using the conventional solid-state method. Microstructure and phase analyses were carried out using scanning electron microscopy (SEM) and X-ray diffraction (XRD) techniques. The improved electrical and magnetic characteristics of BCZT/Sb and CFO/Y materials were the key factors that justified their selection as constituent components for composite fabrication. The measured dielectric permittivity of the composite samples indicated that all composite samples are dielectric. However, the unusually high dielectric loss observed in the composite samples confirmed their conductive nature. Regarding the ferroelectric behavior, saturated P–E loops were observed in composites containing 30 and 40% cobalt ferrite. A further increase in the cobalt ferrite content, however, resulted in leakage current due to the electrical conductivity of the magnetic phase, preventing polarization from reaching saturation. The pure BCZT/Sb ceramic exhibited a high dielectric constant of 4600, a remanent polarization of 8.06 μC/cm², and a saturation polarization of 13.17 μC/cm². Upon incorporation of CFO/Y, the composite with 70 wt% CFO showed a saturation magnetization of 38.49 emu/g, a remanent magnetization of 11.28 emu/g, and a coercive magnetic field of 0.26 kOe. Meanwhile, the ferroelectric coercive field increased from 4.1 kV/cm (BCZT) to 42 kV/cm (BCZT–70CFO), indicating stronger domain pinning. These results confirm the successful integration of ferroelectric and magnetic phases, offering promising potential for magnetoelectric applications.

https://doi.org/10.30501/acp.2025.551238.1185

1. INTRODUCTION

Multiferroic magnetoelectric (ME) materials, which simultaneously display ferroelectric and ferromagnetic properties, have recently attracted significant attention due to their scientific importance and potential applications in innovative multifunctional devices (Liu et al., 2011). The interaction between magnetic and ferroelectric properties in magnetoelectric (ME) materials, known as ME coupling, takes place at the interface between their magnetic and ferroelectric domains (Gorige et al., 2016). The presence of magnetoelectric coupling makes these materials highly suitable for a variety of technological applications. Specifically, they are promising candidates for applications such as electrically written and magnetically read memory technologies, magnetic field ambient

Please cite this article as: Sharifi, A., Hayati, R., Setoudeh, N., & Rezaei, G. (2025). Multiferroic Performance of BCZT/CFO Composites Tailored by Antimony and Yttrium Doping. *Advanced Ceramics Progress*, 11(2), 24-35. https://doi.org/10.30501/acp.2025.551238.1185

sensors, and energy harvesting devices (Naveed-Ul-Haq et al., 2016).

ME materials are broadly categorized into two classes: single-phase multiferroics and composite materials (Wang et al., 2010). Single-phase multiferroic materials, including bismuth ferrite ($BiFeO_3$), exhibit both ferroelectric and ferromagnetic properties within a single material structure (Wang et al., 2020). However, their practical application is often limited due to their low Curie temperature and weak magnetic ordering at room temperature. An alternative approach involves the use of composite multiferroic materials, for example, the combination of lead zirconate titanate (PZT) and cobalt ferrite (CFO) (Ortega et al., 2009). These composites are engineered by combining a ferromagnetic magnetostrictive component with a ferroelectric or piezoelectric component (Gualdi et al., 2024; Kumari et al., 2017; Pradhan et al., 2018). This combination can be achieved in various configurations, such as a granular mixture or a layered structure. The advantage of these composites lies in their potential to generate a strong extrinsic ME effect (Chermahini et al., 2018).

Lead-based ceramics, such as PZT, have long been dominant in piezoelectric applications due to their exceptional piezoelectric performance. However, because of global restrictions on lead-based compounds due to lead toxicity, there is a pressing need to develop suitable alternatives (Negi et al., 2018). $Ba_{0.85}Ca_{0.15}Zr_{0.10}Ti_{0.90}O_3$ (BCZT) ceramic, firstly introduced by Liu and Ren in 2009 (Liu & Ren, 2009), has recently emerged as an attractive lead-free material with exceptional piezoelectric properties comparable to those of lead-based materials (Li et al., 2018; Manohar et al., 2019). Cobalt ferrite ($CoFe_2O_4$) is a widely used magnetic material because of its strong magnetostrictive properties. CFO possesses an inverse spinel crystal structure, which is a key factor contributing to its desirable magnetic properties such as high cubic magneto-crystalline anisotropy, significant saturation magnetization, and notable coercivity (Etier et al., 2015; Kurchania et al., 2015; Majid et al., 2020). Accordingly, researchers have studied the magnetoelectric performance of different types of particulate and laminate BCZT-CFO composites (Kumar et al., 2019; Kumar et al., 2016; Naveed-Ul-Haq et al., 2016; Paul Praveen et al., 2017). Among these studies, Praveen et al. (Paul Praveen et al., 2018) investigated the magnetoelectric coupling effect in layered BCZT–CFO composites through substitutional doping of titanium and cerium oxides in CFO and BCZT compositions, respectively. Their results demonstrated that the incorporation of cerium and yttrium altered the ferroelectric and magnetic properties and improved the magnetoelectric response of the composites. Several other studies have explored BCZT/CFO composites and related multiferroic systems. For example, Negi et al. (Negi et al., 2018) reported dielectric permittivity values around 950 and magnetic saturation of approximately 28 emu/g in lead-free BCZT–CFO composites. Kumar et al. (Kumar et al., 2019) examined the effect of CFO weight fraction and observed moderate ferroelectric and magnetic responses. Praveen et al. (Praveen et al., 2018) introduced Ti and Ce doping in BCZT–CFO laminates, achieving slight improvements in magnetoelectric coupling.

In this study, BCZT was synthesized using the sol-gel method, and CFO powder was prepared via the combustion route. Antimony and yttrium oxides were individually doped into BCZT and CFO, respectively, and, after optimizing the compositions, BCZT/Sb–xCFO/Y composite samples were fabricated. The ferroelectric and magnetic behaviors of these composite samples were subsequently investigated. Although dual-phase doping strategies have been explored in previous studies, the specific combination of antimony in BCZT and yttrium in CFO has not been reported. This unique dopant pairing enables the simultaneous enhancement of ferroelectric and magnetic properties, distinguishing our composite system from those described in the existing literature.

2. Materials and Method

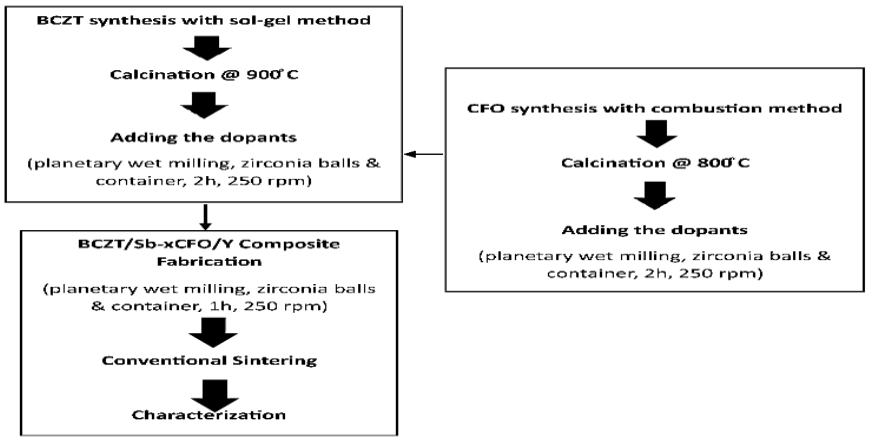

Figure 1. A schematic representation of the experimental procedure.

The experimental procedure is summarized in the Fig. 1 flowchart, and it is clarified in detail in the following:

2.1. Synthesis of cobalt ferrite powder

To prepare cobalt ferrite powder, the combustion synthesis method was employed. The nitrate precursors used included iron(III) nitrate nonahydrate ($Fe(NO_3)_3{\cdot}9H_2O$), cobalt(II) nitrate hexahydrate ($Co(NO_3)_2{\cdot}6H_2O$), and glycine ($C_2H_5NO_2$) as the fuel (purity ≥99%, all obtained from Merck). Based on previous studies (Houshiar et al., 2014; Prabhakaran & Hemalatha, 2016; Sharifi et al., 2021), combustion synthesis can be carried out under three glycine-to-nitrate (G/N) ratio conditions: stoichiometric fuel with a G/N ratio of 1, fuel-rich with a G/N ratio of 1.44, and fuel-deficient conditions. In this study, the fuel-rich reaction with a G/N ratio of 1.44 was utilized.

$$2Fe(NO_3)_3.9H_2O + Co(NO_3)_2.6H_2O + 5.5C_2H_5NO_2 + 4.75O_2 \xrightarrow{\text{yields}} CoFe_2O_4 + 11CO_2 + 37.75H_2O + 6.75N_2 \quad (1)$$

For the synthesis of CFO, 34.4 g of iron nitrate nonahydrate was initially dissolved in deionized water to achieve complete dissolution. Simultaneously, 12.4 g of cobalt nitrate hexahydrate was dissolved in deionized water under similar conditions. Once both solutions were fully dissolved, they were combined, and 17.6 g of glycine was added to the resulting mixture. The solution was then placed on a hot plate stirrer and maintained at 70°C for 15 minutes to ensure complete dissolution of all three components into a homogeneous mixture. Subsequently, stirring was stopped, and the solution was heated to 300°C. Upon evaporation of the deionized water, the mixture underwent combustion from a single ignition point. The combustion reaction was completed in less than 15 minutes, with ignition occurring in under 5 seconds. During combustion, significant amounts of foam were generated, and sparkles appeared at one corner, rapidly spreading throughout the mass to produce a bulky, fluffy product. This synthesis process was followed by an additional heating step at 800°C for 2 hours in air.

2.2. Synthesis of BCZT Powder

The $(Ba_{0.85}Ca_{0.15})(Zr_{0.1}Ti_{0.9})O_3$ powder was synthesized using the sol-gel method. The raw materials used in this process included barium acetate ($Ba(C_4H_6O_4)$, Merck, 99%), calcium acetate ($Ca(C_4H_6O_4)$, Merck, 99%), tetra-n-butyl orthotitanate ($Ti(C_{16}H_{36}O_4)$, Merck, 98%), zirconium propoxide ($Zr(C_{12}H_{28}O_4)$, Merck, 98%), acetylacetone ($C_5H_8O_2$, Merck, 99%), and ammonia solution, which was used to adjust the pH. The procedure is explained in detail in our previous work (Dehnov et al., 2024). At the end of the sol-gel process, a yellow gel was formed, which was subsequently heated at 90°C for 12 hours to convert it into a brown gel. The brown gel was then pulverized into fine powder using a mortar and pestle. Finally, the calcination process was conducted at 900°C for 4 hours.

In the following, 0.1 at.% of antimony and yttrium oxides were incorporated into BCZT and cobalt ferrite powders, respectively, via mechanical alloying. For this purpose, the dopants were added to the powders, which were then milled in a zirconia container with zirconia balls of 3–5 mm diameter in an ethanol medium for 2 hours. A ball-to-powder ratio of 20:1 and a milling speed of 250 rpm were used in a planetary ball mill (Amin Asiya Fanavar, Narya MPM2-250, Iran). The antimony- and yttrium-doped cobalt ferrite compositions were designated CFO/Sb and CFO/Y, respectively, while the Sb- and Y-doped BCZT compositions were labeled BCZT/Sb and BCZT/Y.

2.3. Composite fabrication

After assessing the magnetic and electrical properties, the composite samples were fabricated using CFO/Y and BCZT/Sb powders. Different weight percentages of CFO/Y were incorporated, referred to as BCZT/Sb–xCFO/Y, with x values of 30, 40, 50, 60, and 70 wt%. The powders were mechanically milled in an ethanol medium using a planetary ball mill in a zirconia container with 3–5 mm zirconia balls for 1 hour, maintaining a ball-to-powder weight ratio of 20:1 and a milling speed of 250 rpm. The resulting slurry was dried at 90°C for 12 hours to remove ethanol. The dried composite powders were then sieved through an 80-mesh sieve. The sieved powders were pressed into disk-shaped pellets with a diameter of 10 mm and a thickness of 1 mm by applying an initial pressure of 50 MPa using a steel mold, followed by a final pressure of 250 MPa for 30 seconds using a cold isostatic press (Model 303K CIP, Iran). Finally, the shaped samples were sintered in a high-temperature furnace with a heating rate of 5°C/min over a temperature range of 1200°C to 1300°C for 4 hours.

2.4. Composite characterizations

The phase structure was analyzed using X-ray diffraction (XRD) with a Philips PW 1730 instrument, Netherlands, employing Cu-Kα radiation. Chemical bonding was examined through Fourier-transform infrared (FTIR) spectroscopy using a Shimadzu 8300 spectrometer (Kyoto, Japan). The microstructure and elemental composition of the powders were investigated with a field emission scanning electron microscope (FESEM, MIRA III, Czech Republic). Room-temperature magnetic properties were measured using a

vibrating sample magnetometer (VSM, Daneshpajouh Kashan Company, Iran). For electrical characterization, the samples were coated with silver paste and subsequently heated to 800°C to ensure good ohmic contact. Dielectric properties were determined using a network analyzer (HP 8714C) over a frequency range of 40 Hz to 1 MHz. The ferroelectric behavior of the unpoled samples was assessed via hysteresis loops obtained from a Sawyer-Tower-based ferroelectric tester (Isfahan Technical University, Iran).

3. Results and discussions

Figure 2-a shows the XRD patterns of BCZT and CFO powders, synthesized via the sol-gel and combustion synthesis methods, respectively. As clearly observed, the BCZT powder exhibits a single-phase perovskite structure after calcination at 900 °C, consistent with orthorhombic BaTiO3 (JCPDS no. 96-901-4775, Amm2). The XRD pattern of CFO powder confirms the presence of pure cobalt ferrite with a spinel structure, matching cubic CFO (JCPDS no. 96-591-0064, Fd-3m).

The FTIR spectra of BCZT and CFO powders after synthesis are presented in Figure 2-b. The FTIR spectrum of CFO shows two prominent absorption bands. The first, located around 550–600 cm^{-1}, corresponds to Fe–O and Co–O stretching vibrations in the spinel lattice, involving both octahedral and tetrahedral sites.

The second band, observed near 1100 cm^{-1}, is attributed to residual organic compounds or carbonate impurities, likely originating from the synthesis process.

Nazari et al. (Nazari et al., 2014) studied the structural and magnetic properties of maghemite nanoparticles and reported similar peaks in the FTIR spectrum of iron oxide. In the BCZT spectrum, a prominent peak near 547 cm^{-1} is attributed to Ti–O stretching vibrations along the polar axis. A broad band around 1100 cm^{-1} is likely due to carbonate impurities or residual organic compounds from the synthesis process. Additional weak bands in the range of 1500–1700 cm^{-1} may be associated with bending vibrations of adsorbed water or organic residues. All vibrational assignments have been revised based on the actual FTIR spectrum to ensure clarity and accuracy.

Figure 3 shows the XRD patterns of BCZT/Sb–xCFO/Y composite samples sintered at 1250 °C for 4 hours. Phase identification was performed using X'Pert HighScore software, indicating that the composite samples consisted of tetragonal BaTiO3 with a perovskite structure (JCPDS# 99-901-4669) and spinel-type cobalt ferrite with a cubic structure corresponding to the Fd3m space group (JCPDS# 96-591-0064). In addition, a secondary phase of hexagonal barium ferrite (Ba2Fe24O38, JCPDS# 96-100-8329) was observed in composite samples containing 50–60 wt.% CFO. The XRD pattern of BCZT/Sb–50CFO/Y is shown in Figure 3-d. As clearly seen, apart from the characteristic peaks of BTO and CFO, additional peaks are present, which can be indexed to the barium ferrite secondary phase. The formation of Ba2Fe24O38 is attributed to a solid-state reaction between Ba^{2+} ions from the BCZT matrix and Fe^{3+} ions from the CFO phase during high-temperature sintering. This reaction is more favorable at elevated CFO concentrations, where local diffusion and interfacial reactivity are enhanced.

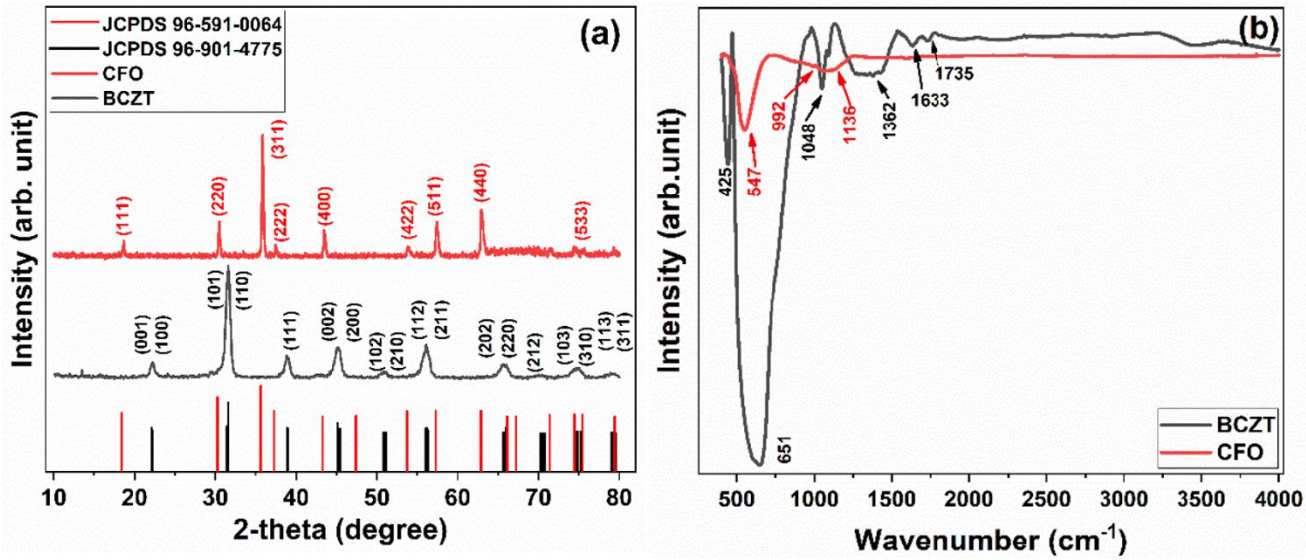

Figure 2. (a) XRD patterns and (b) FTIR spectra of BCZT and CFO powders synthesized with sol-gel and combustion methods, respectively.

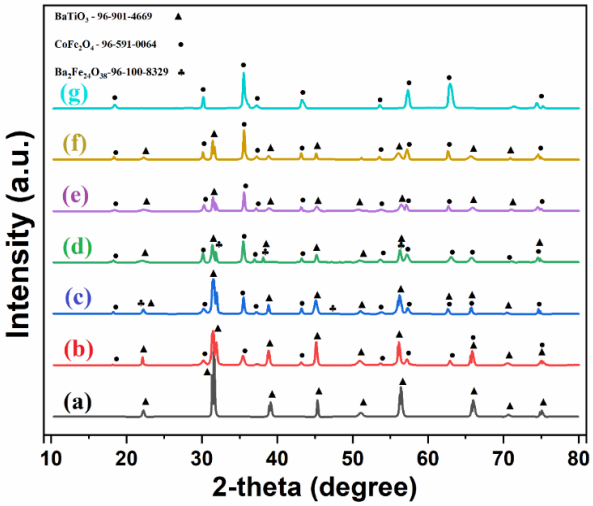

Figure 3. The XRD patterns of BCZT/Sb-xCFO/Y composite samples sinered at 1250 ℃ for 4 h, (a) BCZT/Sb, (b) BCZT/Sb-30CFO/Y, (c) BCZT/Sb-40CFO/Y, (d)BCZT/Sb-50CFO/Y, (e) BCZT/Sb-60CFO/Y, (f) BCZT/Sb-70CFO/Y, (g) CFO/Y.

The SEM micrographs were obtained from the polished and thermally etched surfaces of BCZT/Sb–xCFO/Y composite samples sintered at 1250 °C for 4 hours. The microstructure of BCZT/Sb (Figure 4-a) consists of small grains ranging from 1 to 5 µm. In contrast, the SEM image of the CFO/Y sample (Figure 4-b) shows considerably larger grains, approximately 10 µm in size, compared to BCZT/Sb.

For the composite samples, a bimodal grain size distribution is observed, corresponding to the CFO and BCZT phases. This finding is consistent with the microstructural observations reported by Mane et al. in BCZT–xCFO/Ni composite samples (Mane et al., 2020).

Although quantitative grain size distribution analysis was not performed, qualitative comparison of the SEM images reveals that samples with lower CFO content exhibit more uniform and densely packed grains, suggesting enhanced sintering and higher relative density. In contrast, samples with higher CFO content display increased porosity and irregular grain boundaries,

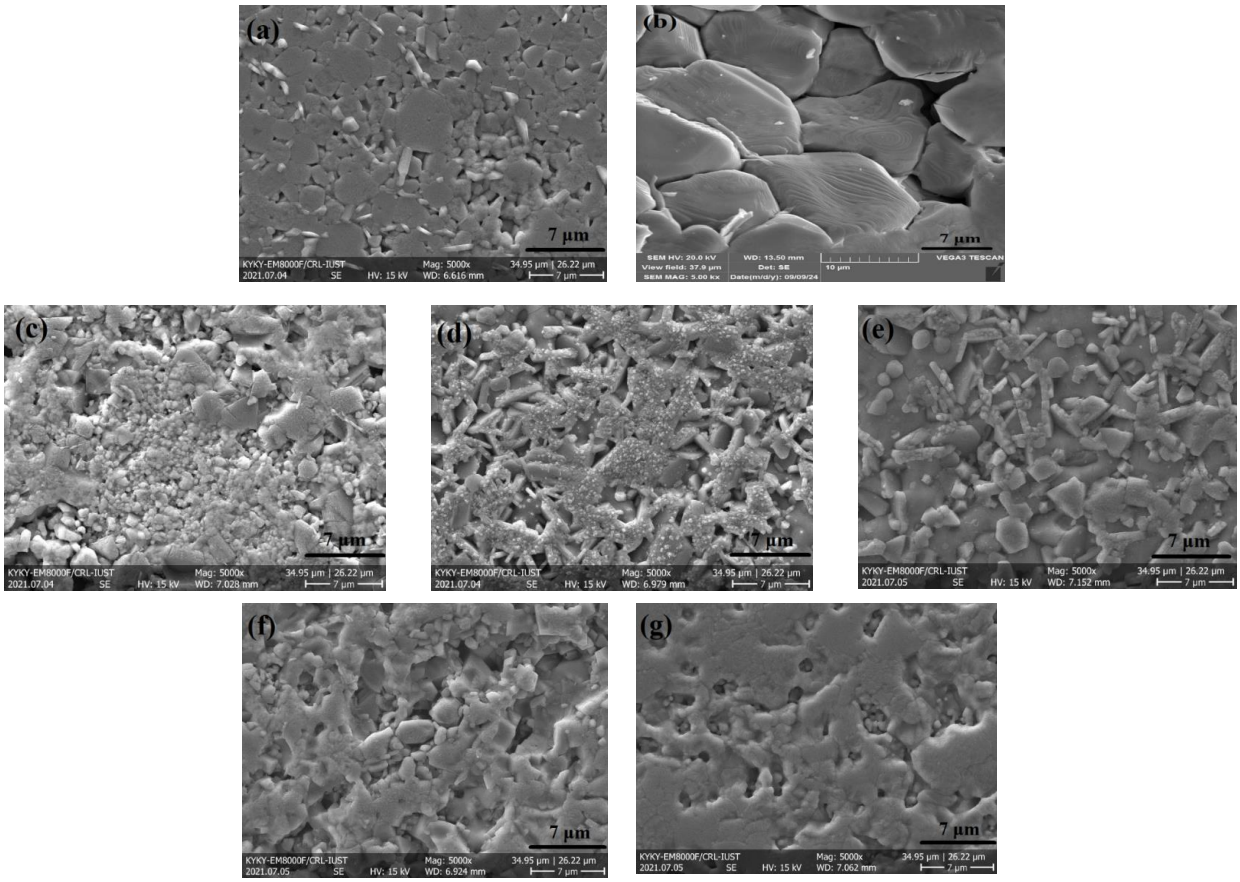

Figure 4. FE-SEM micrographs of BCZT-Sb/xCFO-Y composites, (a) BCZT/Sb, (b) CFO/Y, (c) BCZT/Sb-30CFO/Y, (d)BCZT/Sb-40CFO/Y, (e) BCZT/Sb-50CFO/Y, (f) BCZT/Sb-60CFO/Y, (g) BCZT/Sb-70CFO/Y sintered at 1250 ℃ for 4 h.

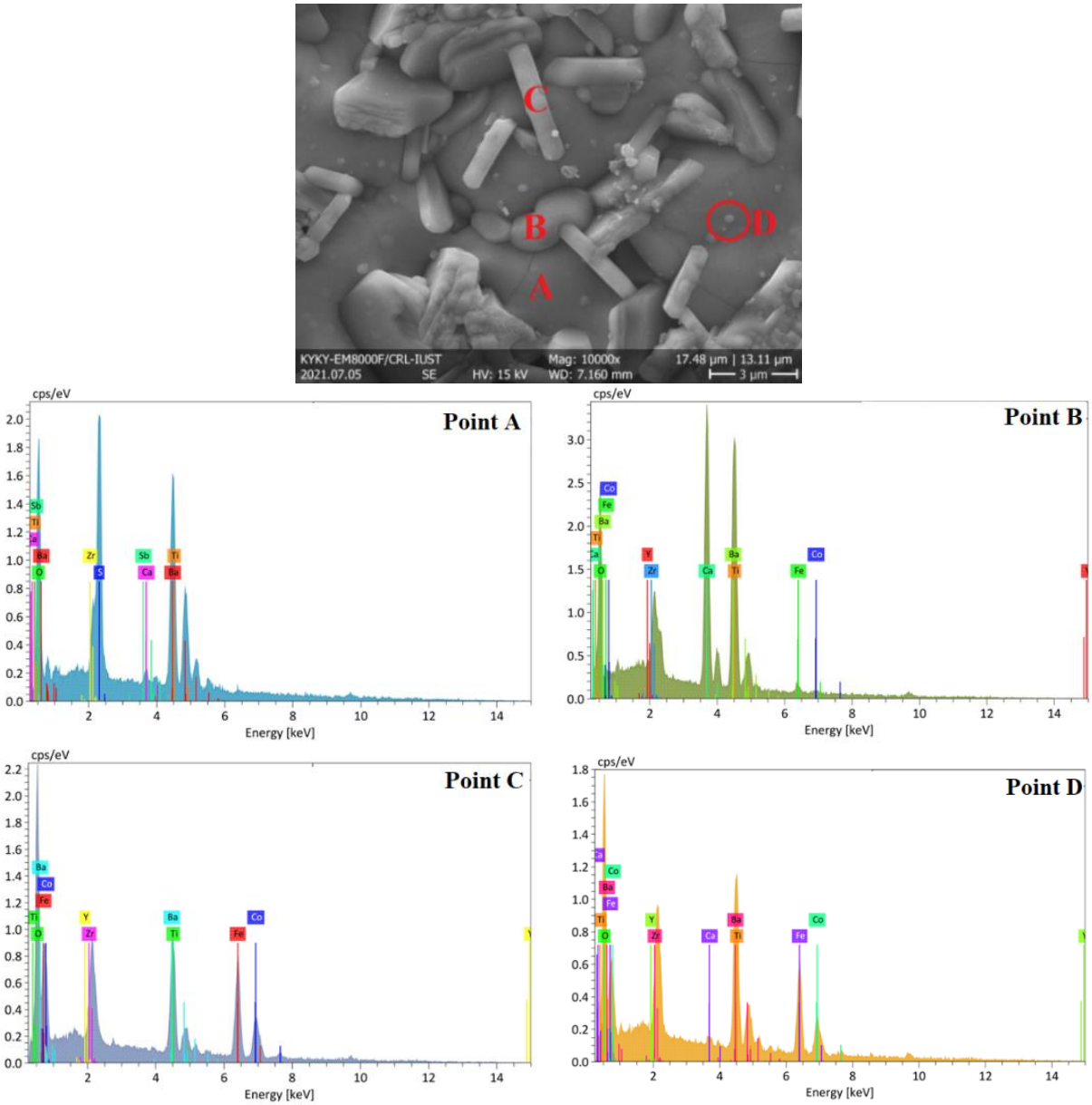

○ **Figure 5.** The SEM image, and the EDS spectra of BCZT/Sb-50CFO/Y sample taken from different points.

indicating inhibited grain growth and reduced densification. These morphological features are consistent with the measured relative density values and support the interpretation of sintering behavior as a function of phase composition.

To further investigate the phase distribution, EDS and elemental mapping were performed on the BCZT/Sb–50CFO/Y composite sample, which contains equal amounts of CFO and BCZT. The EDS spectra were collected from four different points on the SEM image (labeled A–D). The spectra are shown in Figure 5, and the corresponding results are summarized in Table 1. At point A, no Fe or Co ions were detected, and their amounts were negligible at point B, indicating that these points correspond to BCZT-rich regions. Conversely, the EDS results at points C and D show minimal presence of BCZT constituent elements but are rich in CFO elements, identifying these regions as CFO-dominated.

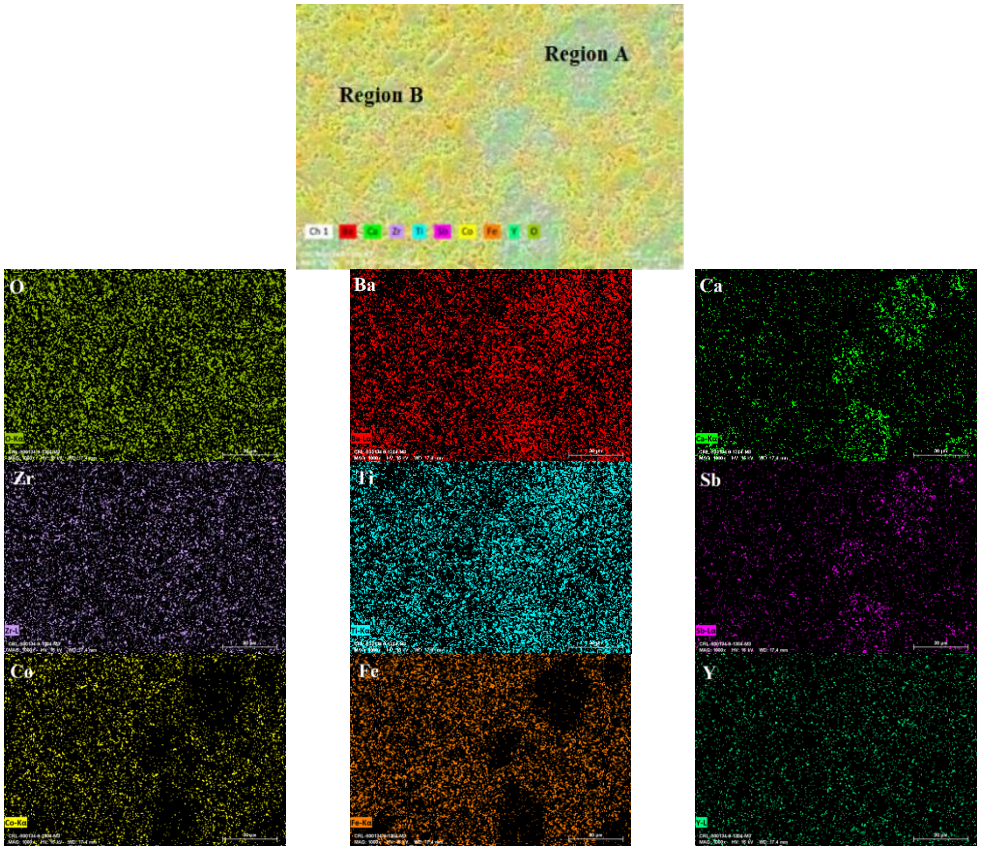

Figure 6. The elemental mapping corresponding to the SEM image of BCZT/Sb-50CFO/Y sample sintered at 1250 ˚C for 4 h.

Table 1. The fraction (at.%) from different points of BCZT/Sb-50CFO/Y composite sample.

Point	Ba	O	Zr	Ti	Ca	Fe	Co	Sb
A	18.74	74.01	2.21	3.71	1.28	-	-	0.048
B	1.07	66.56	1.36	16.32	13.41	0.92	0.36	-
C	2.83	62.41	2.73	7.37	-	16.19	8.47	-
D	4.86	60.91	3.32	10.05	0.62	13.53	6.65	-

Table 2. The data of relative density for BCZT, CFO, and BCZT-xCFO composite samples.

Samples	1200 ˚C	1250 ˚C	1300 ˚C	1350 ˚C	1400 ˚C	1450 ˚C
BCZT-pure	-	-	-	89.5%	92%	94%
BCZT-Sb	-	-	-	91.4%	97.3%	93.5%
BCZT-Y	-	-	-	92.7%	94.8%	92.5%
CFO-pure	-	-	93.1%	84%	-	-
CFO-Sb	-	-	96.4%	92.2%	-	-
CFO-Y	-	-	94.9%	91.1%	-	-
BCZT/Sb-30 CFO/Y	82.7%	92.5%	88.5%	-	-	-
BCZT/Sb-40 CFO/Y	81.4%	89.5%	83%	-	-	-
BCZT/Sb-50 CFO/Y	84.3%	91.4%	82%	-	-	-
BCZT/Sb-60 CFO/Y	83.3%	89.9%	84%	-	-	-
BCZT/Sb-70 CFO/Y	85.7%	93.6%	89.2%	-	-	-

Figure 6 shows the elemental mapping images of the BCZT/Sb–50CFO/Y sample. As observed, region B is rich in Ca ions but depleted of Fe and Co ions. In contrast, region A contains all constituent elements of the BCZT and CFO phases, with the atomic percentage of barium being considerably higher than at the other points.

The relative density data of BCZT/Sb–xCFO/Y composite samples sintered in the temperature range of

1200–1450 °C are summarized in Table 2. Doping BCZT with Sb and Y lowered the sintering temperature of pure BCZT, resulting in a relative density of 97.3% at 1400 °C. Similarly, the addition of yttrium and antimony to CFO reduced its sintering temperature, achieving a high relative density of 96.4% for CFO/Y at 1300 °C. The highest relative densities for BCZT/Sb–xCFO/Y composite samples were obtained at 1250 °C; therefore, this temperature was selected for further studies. These results highlight the significant influence of dopants (antimony and yttrium) on the sintering behavior, as the presence of Sb and Y in BCZT and Y in CFO reduces the temperature required to achieve high relative densities.

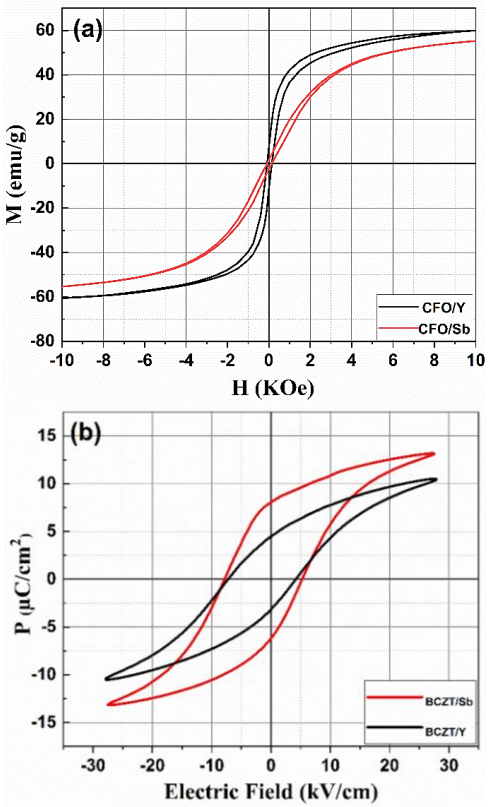

Figure 7. (a) Magnetic hystresis loops of doped-CFO and (b) Ferroelectric hystresis loops of doped-BCZT sintered samples.

Figure 7-a compares the magnetic hysteresis loops of CFO/Sb and CFO/Y samples. The addition of 1 at.% yttrium resulted in improved magnetic behavior compared to antimony-doped cobalt ferrite. Although the coercivity and remanent magnetization of the two compositions were similar, Y-doped CFO exhibited higher saturation magnetization. The magnetic behavior of Y-doped CFO is consistent with previously reported data (Alves et al., 2017). The ferroelectric behavior of Y- and Sb-doped BCZT samples is shown in Figure 7-b. In Sb-doped BCZT, the remanent and saturation polarization values are higher than in Y-doped BCZT, in agreement with earlier reports (Parjansri et al., 2016). Based on these results, BCZT/Sb and CFO/Y compositions were selected for the fabrication of BCZT/Sb–xCFO/Y multiferroic composite samples.

The magnetic hysteresis loops of BCZT/Sb–xCFO/Y composite samples are illustrated in Figure 8-a, and the corresponding magnetic properties, including saturation magnetization, remanent magnetization, and coercive field, are summarized in Table 3. As observed from Figure 8-a, with increasing volume fraction of the ferroelectric phase, the saturation magnetization of the composite decreases linearly. This reduction is primarily due to the dilution effect caused by the incorporation of the non-magnetic piezoelectric phase into the magnetic phase. Furthermore, each ferrite particle is increasingly isolated by the adjacent ferroelectric phase, reducing magnetic connectivity and thereby lowering coercivity. The remanent magnetization also decreases with increasing BCZT content, reflecting the diminished contribution of the magnetic phase to the overall composite magnetization. This reduction in Mr indicates that the composite's ability to retain magnetization after removal of an external magnetic field diminishes as the ferroelectric phase becomes more dominant, which may have important implications for applications requiring stable magnetic memory or sensing capabilities.

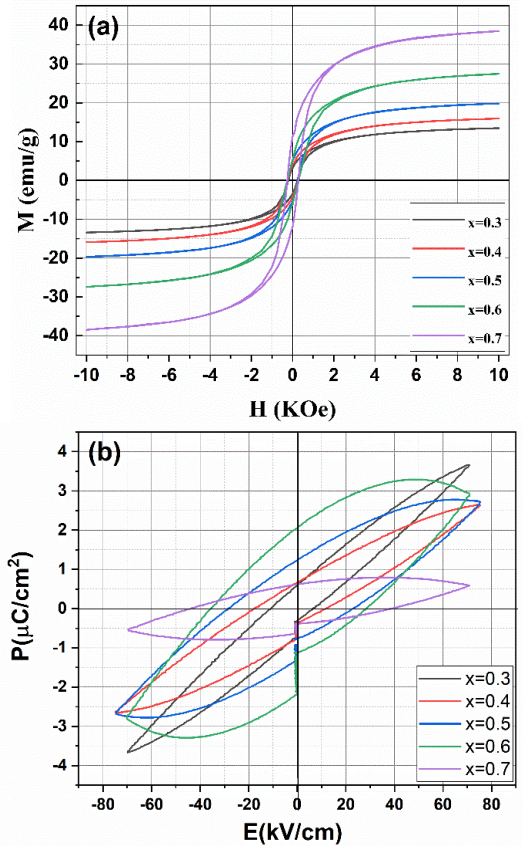

Figure 8. (a) Ferroelectric and (b) magnetic hysteresis loops of BCZT/Sb-xCFO/Y composite samples.

Alternatively, the incorporation of BCZT particles can be considered equivalent to introducing pores within the composite, leading to a reduction in the magnetic moment per unit volume and, consequently, lowering the saturation magnetization (Narendra Babu et al., 2009). A slight variation in the coercive magnetic field of the composite samples was also observed, consistent with the results reported by Negi et al. (Negi et al., 2018). These changes in magnetic properties with varying BCZT content underscore the importance of phase composition in tailoring the multifunctional behavior of these composites. By carefully controlling the ratio of ferroelectric to magnetic phases, it is possible to optimize the composite for specific applications, such as magnetoelectric sensors, actuators, or energy-harvesting devices. The interplay between the ferroelectric and magnetic phases offers opportunities to explore novel phenomena, such as strain-mediated magnetoelectric coupling, which could lead to the development of advanced multifunctional materials with enhanced performance.

Another important magnetic parameter is the squareness ratio (Mr/Ms), which was also calculated for the composite samples in this study. A higher squareness ratio indicates a more square-shaped hysteresis loop, reflecting higher remanent magnetization and a more stable magnetic state. As shown in Table 3, the maximum squareness ratio of 0.26 was obtained for the BCZT/Sb–70CFO/Y composite, which also exhibited the largest saturation and remanent magnetization values among the composites. Notably, even samples with a higher proportion of the ferroelectric phase displayed slightly lower values, with a high squareness of 0.26 observed in the composite containing 40 wt.% CFO/Y.

The magnetic properties of the BCZT/Sb–CFO/Y composites in this study were compared with those of layered BCZT/Ce–CFO/Ti multiferroic composites reported by Praveen et al (Paul Praveen et al., 2018). The improved multiferroic performance of the layered BCZT/Ce–CFO/Ti composite was attributed to microstructural modifications and enhancements in the ferroelectric and magnetic properties of the constituent phases. In addition to the dilution effect and leakage caused by the magnetic phase, the formation of $Ba_2Fe_{24}O_{38}$ may further influence the composite's properties. As a hard magnetic phase, it can locally increase coercivity while reducing overall saturation magnetization due to phase dilution. Its conductive nature may also enhance leakage current and disrupt ferroelectric domain switching, particularly in samples with higher CFO content. These effects highlight the importance of phase purity and microstructural control in optimizing the multifunctional performance of such composites.

This comparison provides valuable insights into the effects of doping on the multiferroic behavior of the composite. In the layered BCZT/Ce–CFO/Ti composite, the ferroelectric and ferromagnetic properties were not significantly altered by the addition of cerium and titanium dopants. However, the presence of these dopants led to a substantial increase in the multiferroic coefficients compared to the undoped composite.

Figure 8-b shows the room-temperature ferroelectric hysteresis loops of the BCZT/Sb–CFO/Y composite samples. In composites containing 30 and 40 wt.% CFO/Y, the hysteresis loops reached saturation. However, with increasing CFO/Y content, the loops did not achieve saturation polarization due to leakage current. The leaky behavior of these samples can be attributed to the presence of the conductive magnetic phase. At lower CFO contents, the CFO particles are surrounded by high-resistance ferroelectric particles, which effectively block conduction pathways within the microstructure, resulting in low overall conductivity and reduced leakage current (Bai et al., 2007). Despite the presence of abnormal hysteresis loops, the increase in coupling-related parameters, such as coercive field and remnant polarization, with higher ferrite content indicates significant magnetoelectric coupling in the multiferroic composites (Mane et al., 2020).

Table 3. Magnetic parameters obtained from the magnetic hystresis loops of pure and doped CFO and BCZT/Sb-xCFO/Y composite samples.

Samples	Saturation Magnetization (emu/g)	Remenant Magnetization (emu/g)	Mr/Ms	Coercive Field (kOe)
CFO-Y	59.98	7.02	0.11	0.151
CFO-Sb	55.28	1.6	0.02	0.134
CFO	57.93	4.59	0.07	0.133
BCZT/Sb-30 CFO/Y	13.47	3.21	0.23	0.21
BCZT/Sb -40 CFO/Y	15.96	4.16	0.26	0.24
BCZT/Sb -50 CFO/Y	19.84	5.02	0.25	0.24
BCZT/Sb -60 CFO/Y	27.48	5.23	0.19	0.26
BCZT/Sb -70 CFO/Y	38.49	11.28	0.29	0.26

Table 4. Summary of ferroelectric parameters obtained from the ferroelectric hystresis loops.

Samples	Saturation Polarization	Remanent Polarization	Coercive Field (kV/cm)
BCZT	10.51	4.47	4.1
BCZT/Sb	13.17	8.06	5.3
BCZT 70-30 CFO	3.66	0.59	9
BCZT 60-40 CFO	2.58	0.59	14
BCZT 50-50 CFO	2.70	1.24	25.5
BCZT 40-60 CFO	3.29	2.06	31.5

The characteristic parameters of the ferroelectric loops are summarized in Table 4. Both the remnant polarization and coercive field increase with increasing CFO content in the composite. The rise in coercive field suggests that the ferrite components within the ferroelectric matrix impede ferroelectric domain motion, effectively pinning the domains (Rani et al., 2014). Consequently, the simultaneous presence of ferroelectricity and ferromagnetism in the hysteresis loops of BCZT/Sb–xCFO/Y composites confirm their multiferroic nature.

Figure 9 shows the variation of dielectric constant and loss factor as a function of cobalt ferrite content. The BCZT/Sb sample exhibits a high dielectric constant of 4600, which decreases significantly with the addition of the magnetic phase. Nevertheless, even composites with high CFO content retain a substantial dielectric constant, reaching 139 for BCZT/Sb–70CFO/Y. The dielectric loss factor of the BCZT/Sb sample is as low as 0.04; however, it increases markedly with higher CFO content. This rise in dielectric loss is attributed to the electrical conductivity of the magnetic phase, indicating the presence of leakage current within the composites.

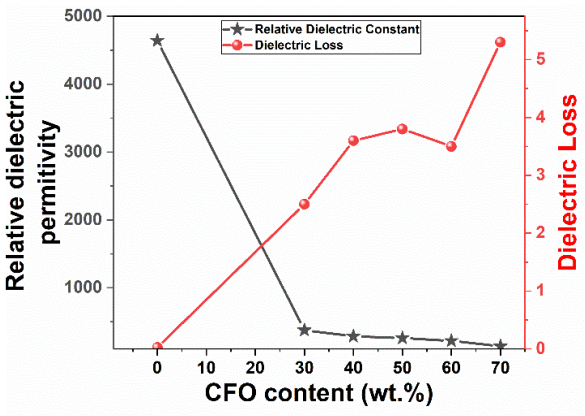

Figure 9. Variations in room-temperature dielectric properties of BCZT/Sb-xCFO/Y composite samplesmeasured at 1kHz frequency.

The increase in dielectric loss factor (tan δ) with higher CFO content, as shown in Figure 9, provides indirect evidence of enhanced leakage current in the composite samples. This behavior is attributed to the conductive nature of the magnetic phase, which facilitates the formation of local conduction paths. The reduction in dielectric constant and the distortion of P–E loops in these samples further support the presence of leakage mechanisms, particularly at elevated CFO concentrations.

Figure 10 presents the variation of dielectric constant with frequency over the range of 40 Hz to 1 MHz. For all compositions, the dielectric constant decreases with increasing frequency up to 1 kHz and then stabilizes at higher frequencies. A resonance phenomenon was observed in the BCZT/Sb–70CFO/Y sample within the frequency range of 300–400 kHz, which is attributed to the stronger piezoelectric properties of this composition.

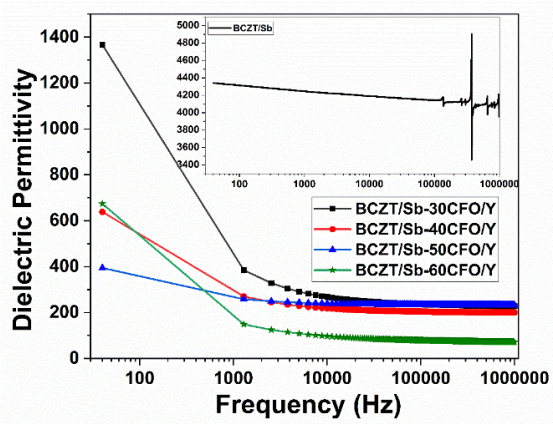

Figure 10. The logarithmic plots of dielectric permittivity versus frequency for BCZT/Sb and BCZT/Sb-xCFO/Y composites.

Table 5 presents a comparative overview of key multifunctional parameters for previously reported multiferroic composites and the current study. The BCZT/Sb–40CFO/Y composition exhibits a balanced profile, with Ms = 15.96 emu/g, Mr = 4.16 emu/g, Pr = 2.06 μC/cm², and εr ≈ 360. In contrast, BCZT/Sb–70CFO/Y offers superior magnetic performance (Ms = 38.49 emu/g, Mr = 11.28 emu/g) but shows reduced ferroelectric and dielectric properties. Compared to literature values, both compositions demonstrate competitive or enhanced performance, confirming the effectiveness of Sb doping and CFO/Y incorporation. The inclusion of remanent magnetization (Mr) further emphasizes the magnetic stability of these composites, which is crucial for memory and magnetoelectric applications.

Table 5. Comparative multifunctional properties of BCZT-based magnetoelectric composites reported in literature and this work.

Composition / Study	Ms (emu/g)	Mr (emu/g)	Pr (μC/cm²)	εr	tan δ	Reference
BCZT/Sb–40CFO/Y (This work)	15.96	4.16	2.06	~360	~3.4	—
BCZT/Sb–70CFO/Y (This work)	38.49	11.28	0.59	~300	~5.5	—
(1−x)BCZT–xCFO	25.6	—	2.1	120	—	Praveen et al., 2017
BT–15%CFO	18.3	—	—	95	—	Etier et al., 2015
BCZT–NZFO	22.0	—	1.8	110	—	Negi et al., 2018
BZT–BCT/NFO	30.2	—	—	105	—	Rani et al., 2014

4. Conclusion

This study investigated the effects of antimony and yttrium oxides on the electrical and magnetic properties of two key materials: Ba0.85Ca0.15Zr0.10Ti0.90O3 (BCZT) and CoFe2O4 (CFO). The constituent materials were synthesized using chemical methods, and the composites were fabricated via a conventional solid-state process. The main findings are as follows:

1. The incorporation of antimony and yttrium dopants enhanced the electrical and magnetic properties of BCZT and CFO, respectively.

2. The BCZT/Sb and CFO/Y composites exhibited high dielectric permittivity alongside elevated dielectric loss, indicating a conductive character. The composites demonstrated ferroelectric behavior, with saturated P–E loops observed at specific dopant concentrations. However, increasing the cobalt ferrite content induced leakage current due to the conductivity of the magnetic phase, preventing full polarization saturation.

3. All composites displayed magnetic behavior, confirming their potential as multiferroic materials owing to their combined electrical and magnetic properties.

Acknowledgement

This research was conducted as part of the comprehensive research plan of the corresponding author. The authors gratefully acknowledge the Deputy of Research of Yasouj University for their financial support. The authors also extend their appreciation to the Central Laboratory of Yasouj University for providing the facilities and equipment necessary to carry out this study.

Research ethics

Not applicable.

Informed consent

Not applicable.

Author contributions

All authors have accepted responsibility for the entire content of this manuscript and approved its submission.

- **Ali Sharifi:** Carrying out measurements, Data curation.
- **Raziye Hayati:** Conceptualization, Supervision, Visualization, Resources, Methodology, Writing-Original draft preparation, Reviewing & Editing.
- **Nader Setoudeh**: Supervision, Reviewing & Editing.
- **Ghasem Rezaei**: Reviewing & Editing.

Use of LLM, AI and MLT

None declared.

Conflicts of interest

All other authors state no conflict of interest.

Research Funding

Yasouj University, Grant No. 18563.

Data and code availability

The datasets generated during and/or analyzed during the current study are available from the corresponding author on reasonable request.

References

1. Alves, T. E. P., Pessoni, H. V. S., & Franco Jr, A. (2017). The effect of Y^{3+} substitution on the structural, optical band-gap, and magnetic properties of cobalt ferrite nanoparticles [10.1039/C7CP02167D]. *Physical Chemistry Chemical Physics*, *19*(25), 16395-16405. https://doi.org/10.1039/C7CP02167D
2. Bai, Y., Zhou, J., Gui, Z., Li, L., & Qiao, L. (2007). A ferromagnetic ferroelectric cofired ceramic for hyperfrequency. *Journal of Applied Physics*, *101*(8). https://doi.org/10.1063/1.2714005
3. Chermahini, M. D., Shahraki, M. M., & Kazazi, M. (2018). Multiferroic properties of novel lead-free KNN-LT/20NZCFO magneto-electric composites. *Materials Letters*, *233*, 188-190. https://doi.org/10.1016/j.matlet.2018.09.001
4. Dehnov, F. Z., Hayati, R., & Tayebi, L. (2024). Studying the electrical, mechanical, and biological properties of BCZT–HA composites. *Journal of Biomedical Materials Research Part B: Applied Biomaterials*, *112*(3), e35392. https://doi.org/10.1002/jbm.b.35392
5. Etier, M., Schmitz-Antoniak, C., Salamon, S., Trivedi, H., Gao, Y., Nazrabi, A., Landers, J., Gautam, D., Winterer, M., Schmitz, D., Wende, H., Shvartsman, V. V., & Lupascu, D. C. (2015). Magnetoelectric coupling on multiferroic cobalt ferrite–barium titanate ceramic composites with different connectivity schemes. *Acta Materialia*, *90*, 1-9. https://doi.org/10.1016/j.actamat.2015.02032
6. Gorige, V., Kati, R., Yoon, D. H., & Anil Kumar, P. S. (2016). Strain mediated magnetoelectric coupling in a NiFe2O4–BaTiO3 multiferroic composite. *Journal of Physics D: Applied Physics*, *49*(40), 405001. https://doi.org/10.1088/0022-3727/49/40/405001
7. Gualdi, A. J., Dos Santos Batacline, L., Correia Espírito Santo, G., Alkathy, M. S., & Zabotto, F. L. (2024). Synthesis and high-frequency magnetoelectric characterization of the 0–3 particulate lead-free multiferroic composite KNN/CFO. *Journal of Physics:*

Condensed Matter, *36*(33), 335703. https://doi.org/10.1088/1361-648X/ad48f0

8. Houshiar, M., Zebhi, F., Razi, Z. J., Alidoust, A., & Askari, Z. (2014). Synthesis of cobalt ferrite (CoFe2O4) nanoparticles using combustion, coprecipitation, and precipitation methods: A comparison study of size, structural, and magnetic properties. *Journal of Magnetism and Magnetic Materials*, *371*, 43-48. https://doi.org/10.1016/j.jmmm.2014.06.059
9. Kumar, A. S., Lekha, C. S. C., Vivek, S., Nandakumar, K., Anantharaman, M. R., & Nair, S. S. (2019). Effect of CoFe2O4 weight fraction on multiferroic and magnetoelectric properties of $(1-x)Ba_{0.85}Ca_{0.15}Zr_{0.1}Ti_{0.9}O_3 - xCoFe_2O_4$ particulate composites. *Journal of Materials Science: Materials in Electronics*, *30*(9), 8239-8248. https://doi.org/10.1007/s10854-019-01140-3
10. Kumar, A. S., Lekha, C. S. C., Vivek, S., Saravanan, V., Nandakumar, K., & Nair, S. S. (2016). Multiferroic and magnetoelectric properties of $Ba_{0.85}Ca_{0.15}Zr_{0.1}Ti_{0.9}O_3$–$CoFe_2O_4$ core–shell nanocomposite. *Journal of Magnetism and Magnetic Materials*, *418*, 294-299. https://doi.org/10.1016/j.jmmm.2016.02.065
11. Kumari, M., Prakash, C., & Chatterjee, R. (2017). Room temperature large self-biased magnetoelectric effect in non-lead based piezoelectric and magnetostrictive (0−3) particulate composite system. *Journal of Magnetism and Magnetic Materials*, *429*, 60-64. https://doi.org/10.1016/j.jmmm.2017.01.010
12. Kurchania, R., Rathore, D., & Pandey, R. K. (2015). Size dependent strain and nanomagnetism in $CoFe_2O_4$ nanoparticles. *Journal of Materials Science: Materials in Electronics*, *26*(12), 9355-9365. https://doi.org/10.1007/s10854-015-3083-3
13. Li, S. B., Wang, C. B., Shen, Q., & Zhang, L. M. (2018). Multiferroic properties of (1-x)BCZT-xLCMO laminated composites. *Ceramics International*, *44*(1), 231-235. https://doi.org/10.1016/j.ceramint.2017.09.163
14. Liu, W., & Ren, X. (2009). Large piezoelectric effect in Pb-free ceramics. *Phys Rev Lett*, *103*(25), 257602. https://doi.org/10.1103/PhysRevLett.103.257602
15. Liu, Y., Ruan, X., Zhu, B., Chen, S., Lu, Z., Shi, J., & Xiong, R. (2011). $CoFe_2O_4$/$BaTiO_3$ Composites via Spark Plasma Sintering with Enhanced Magnetoelectric Coupling and Excellent Anisotropy. *Journal of the American Ceramic Society*, *94*(6), 1695-1697. https://doi.org/10.1111/j.1551-2916.2011.04582.x
16. Majid, F., Nazir, A., Ata, S., Bibi, I., Mehmood, H. S., Malik, A., Ali, A., & Iqbal, M. (2020). Effect of Hydrothermal Reaction Time on Electrical, Structural and Magnetic Properties of Cobalt Ferrite. *Zeitschrift für Physikalische Chemie*, *234*(2), 323-353. https://doi.org/doi:10.1515/zpch-2019-1423
17. Mane, S. M., Nimbalkar, A. R., Kim, H., Kulkarni, S. B., Tayade, N. T., Thombare, J. V., Dhasade, S. S., & Shin, J. C. (2020). Magnetoelectric and magnetodielectric coupling in partially Ni-doped $CoFe_2O_4$ and $0.15(Ba_{0.7}Ca_{0.3}TiO_3)$–$0.85(BaZr_{0.2}Ti_{0.8}O_3)$ composites prepared via clean microwave sintering. *Journal of Alloys and Compounds*, *849*, 156599. https://doi.org/10.1016/j.jallcom.2020.156599
18. Manohar, C. S., Kumar, B. S., Sadhu, S. P. P., Srimadh, S. K., Muthukumar, V. S., Venketesh, S., & Varma, K. B. R. (2019). Novel Lead-free biocompatible piezoelectric Hydroxyapatite (HA) – BCZT ($Ba_{0.85}Ca_{0.15}Zr_{0.1}Ti_{0.9}O_3$) nanocrystal composites for bone regeneration. Nanotechnology Reviews, *8*(1), 61-78. https://doi.org/doi:10.1515/ntrev-2019-0006
19. Narendra Babu, S., Suryanarayana, S. V., & Bhimasankaram, T. (2009). Magnetic and magnetoelectric characterization of $Ni_{0.93}Co_{0.02}Mn_{0.05}Fe_{1.95}O_4$ and PZT composites. *Journal of Alloys and Compounds*, *473*(1), 418-422. https://doi.org/10.1016/j.jallcom.2008.05.097
20. Naveed-Ul-Haq, M., Shvartsman, V. V., Salamon, S., Wende, H., Trivedi, H., Mumtaz, A., & Lupascu, D. C. (2016). A new (Ba, Ca) (Ti, Zr)O_3 based multiferroic composite with large magnetoelectric effect. *Scientific Reports*, *6*(1), 32164. https://doi.org/10.1038/srep32164
21. Nazari, M., Ghasemi, N., Maddah, H., & Motlagh, M. M. (2014). Synthesis and characterization of maghemite nanopowders by chemical precipitation method. *Journal of Nanostructure in Chemistry*, *4*(2), 99. https://doi.org/10.1007/s40097-014-0099-9
22. Negi, N. S., Kumar, R., Sharma, H., Shah, J., & Kotnala, R. K. (2018). Structural, multiferroic, dielectric and magnetoelectric properties of $(1-x)Ba_{0.85}Ca_{0.15}Ti_{0.90}Zr_{0.10}O_3$-$(x)CoFe_2O_4$ lead-free composites. *Journal of Magnetism and Magnetic Materials*, *456*, 292-299. https://doi.org/https://doi.org/10.1016/j.jmmm.2017.12.095
23. Ortega, N., Kumar, A., Katiyar, R. S., & Rinaldi, C. (2009). Dynamic magneto-electric multiferroics PZT/CFO multilayered nanostructure. *Journal of Materials Science*, *44*(19), 5127-5142. https://doi.org/10.1007/s10853-009-3635-0
24. Parjansri, P., Intatha, U., Guo, R., Bhalla, A. S., & Eitssayeam, S. (2016). Effect of Sb_2O_3 on the electrical properties of $Ba_{0.9}Ca_{0.1}Zr_{0.1}Ti_{0.9}O_3$ ceramics fabricated using nanocrystals seed. *Applied Physics A*, *122*(9), 840. https://doi.org/10.1007/s00339-016-0320-4
25. Paul Praveen, J., Monaji, V. R., Chandrakala, E., Indla, S., Dinesh kumar, S., Subramanian, V., & Das, D. (2018). Enhanced magnetoelectric coupling in Ti and Ce substituted lead free CFO-BCZT laminate composites. *Journal of Alloys and Compounds*, *750*, 392-400. https://doi.org/10.1016/j.jallcom.2018.04.026
26. Paul Praveen, J., Reddy, M. V., Kolte, J., Dinesh Kumar, S., Subramanian, V., & Das, D. (2017). Synthesis, characterization, and magneto-electric properties of (1−x)BCZT-CFO ceramic particulate composites. *International Journal of Applied Ceramic Technology*, *14*(2), 200-210. https://doi.org/https://doi.org/10.1111/ijac.12640
27. Prabhakaran, T., & Hemalatha, J. (2016). Combustion synthesis and characterization of cobalt ferrite nanoparticles. *Ceramics International*, *42*(12), 14113-14120. https://doi.org/10.1016/j.ceramint.2016.06.025
28. Pradhan, L. K., Pandey, R., Kumar, R., & Kar, M. (2018). Lattice strain induced multiferroicity in PZT-CFO particulate composite. *Journal of Applied Physics*, *123*(7). https://doi.org/10.1063/1.5008607
29. Rani, J., Yadav, K. L., & Prakash, S. (2014). Dielectric and magnetic properties of $xCoFe_2O_4$–$(1-x)[0.5Ba(Zr_{0.2}Ti_{0.8})O_3$–$0.5(Ba_{0.7}Ca_{0.3})TiO_3]$ composites. *Materials Research Bulletin*, *60*, 367-375. https://doi.org/10.1016/j.materresbull.2014.09.013
30. Sharifi, A., Hayati, R., Setoudeh, N., & Rezaei, G. (2021). A comparison between structural and magnetic behavior of cobalt ferrite synthesized via solid state and chemical methods. *Materials Research Express*, *8*, 106103. https://doi.org/10.1088/2053-1591/ac29f7
31. Wang, N., Luo, X., Han, L., Zhang, Z., Zhang, R., Olin, H., & Yang, Y. (2020). Structure, Performance, and Application of BiFeO3 Nanomaterials. *Nano-Micro Letters*, *12*(1), 81. https://doi.org/10.1007/s40820-020-00420-6
32. Wang, Y., Hu, J., Lin, Y., & Nan, C.-W. (2010). Multiferroic magnetoelectric composite nanostructures. *NPG Asia Materials*, *2*(2), 61-68. https://doi.org/10.1038/asiamat.2010.32